


Evolution of vortical structures in a curved artery model with non-Newtonian blood-analog fluid under pulsatile inflow conditions

Mohammad Reza Najjari¹ · Michael W. Plesniak^{1,2} 

Received: 26 February 2016 / Revised: 6 May 2016 / Accepted: 16 May 2016 / Published online: 31 May 2016
© Springer-Verlag Berlin Heidelberg 2016

Abstract Steady flow and physiological pulsatile flow in a rigid 180° curved tube are investigated using particle image velocimetry. A non-Newtonian blood-analog fluid is used, and in-plane primary and secondary velocity fields are measured. A vortex detection scheme (d_2 -method) is applied to distinguish vortical structures. In the pulsatile flow case, four different vortex types are observed in secondary flow: deformed-Dean, Dean, Wall and Lyne vortices. Investigation of secondary flow in multiple cross sections suggests the existence of vortex tubes. These structures split and merge over time during the deceleration phase and in space as flow progresses along the 180° curved tube. The primary velocity data for steady flow conditions reveal additional vortices rotating in a direction opposite to Dean vortices—similar to structures observed in pulsatile flow—if the Dean number is sufficiently high.

1 Introduction

For roughly a century, fluid flow through a curved pipe has been investigated in many studies because of its many applications—from industrial to physiological flows. Dean (1927, 1928) analytically showed that one symmetric counter-rotating vortex pair forms in steady flow in curved pipes. He also established a non-dimensional

number, subsequently called the Dean number (De). His analytical solution based on perturbation theory was limited to low De , which was expanded by other studies that varied De and found its effects on the flow structures. Subsequently, Lyne (1971) theoretically proved one extra pair of vortices, rotating in opposite direction of Dean vortices in fully developed oscillatory flow, in a curved tube with high Womersley number ($\alpha > 13$). Lyne's flow visualization and other studies (Zalosh and Nelson 1973; Bertelsen 1975; Mullin and Greated 1980; Eckmann and Grotberg 1988) also confirmed his theory. Later, Sudo et al. (1992) studied pulsatile flow in curved pipes over a wide range of Womersley number and classified the secondary flow structures into five categories (Dean; deformed-Dean; intermediate between Dean and Lyne; Lyne; and deformed-Lyne). Berger et al. (1983) published a detailed literature review on flow in curved pipes.

Due to difficulties in performing experiments, many studies have employed numerical simulations or analytical approaches to investigate the physics of the flow in curved tubes (Zalosh and Nelson 1973; Soh and Berger 1984; Hamakiotes and Berger 1988; Shahcheraghi et al. 2002; Siggers and Waters 2005). Hamakiotes and Berger (1988) simulated the pulsatile flow using a computational fluid dynamics (CFD) projection method. They showed that for high Dean numbers the secondary flow separates from the inner wall and a small vortex forms in the separation region. Hamakiotes and Berger (1988) also indicated that the pressure leads the velocity (in phase), and this causes a flow reversal near the pipe wall, and hence, a local maximum in axial shear stress occurs. Zalosh and Nelson (1973) analytically solved the flow in a curved pipe under oscillatory pressure gradient and showed that for greater frequencies the inviscid core is surrounded by a viscous boundary layer confined to the wall region. Under these conditions,

✉ Michael W. Plesniak
plesniak@gwu.edu

¹ Biofluid Dynamics Laboratory, The George Washington University, 800 22nd St. NW, Washington, DC, USA

² Department of Mechanical and Aerospace Engineering, The George Washington University, 800 22nd St. NW, Washington, DC 20052, USA

they observed a doubly peaked axial velocity profile and hence, a negative centrifugal force gradient, which led to secondary flow being directed toward the inner wall, opposite to the direction of the Dean vortex. This counter-rotating vortex pair is the Lyne vortex system (Lyne 1971). Soh and Berger (1984) simulated steady flow using an artificial compressibility method and, interestingly, observed similar axial velocity profiles as in the pulsatile case. They reported a two-step plateau in axial velocity for high Dean numbers ($Re\sqrt{\delta} = 564.8$ and 680.3) due to separation of secondary flow from the inner wall and existence of inviscid core region and doubly peaked axial velocity due to highly distorted secondary flow. Therefore, the doubly peaked axial velocity accompanied with a negative centrifugal force gradient can occur in steady flows at sufficiently high Dean numbers, as well as in pulsatile flows.

Experimental studies on flow in curved pipes can provide a basis for evaluation of simulations and insights into flow dynamics. Chandran and Yearwood (1981) studied physiological pulsatile flow in a curved pipe using three-dimensional hot-film anemometry. They reported shifting in peak axial velocity along the curve, reversed flow along the inner wall during the deceleration phase and trapped vortical motion downstream of the inlet. The separation from the inner wall was also reported by Talbot and Gong (1983) who measured a pulsatile sinusoidal flow in curved pipes with two curvature ratios ($\delta = 1/20$ and $1/7$) under different Womersley numbers using a laser velocimetry technique. They noted that when curvature ratio is high the primary flow tends to separate from the inner wall due to adverse pressure gradient imposed by wall curvature and flow deceleration. Furthermore, Talbot and Gong (1983) observed the separation point moving upstream during flow deceleration. Similar to Chandran and Yearwood (1981), they reported reversed flow at the inner wall, but observed less shifting and variation in maximum of axial velocity profile.

Advances in computational resources and developments in experimental instrumentation have overcome the limitations in previous studies and provided simulations with higher spatial resolution, as well as high spatial resolution planar flow-field measurement (Boiron et al. 2007; Huang et al. 2010; Timité et al. 2010; Jarrahi et al. 2011). Boiron et al. (2007), for example, studied several pulsatile physiological flow rates both numerically and experimentally and obtained good agreement between these results. The axial velocity peak in their flow at the 90° location was located near the inner wall during acceleration and shifted toward the outer wall, with a higher maximum during inflow deceleration. They also computed numerous forces in the flow field based on their numerical results, including radial pressure gradient force, centrifugal force and spatial and temporal inertial forces. They showed that the radial pressure

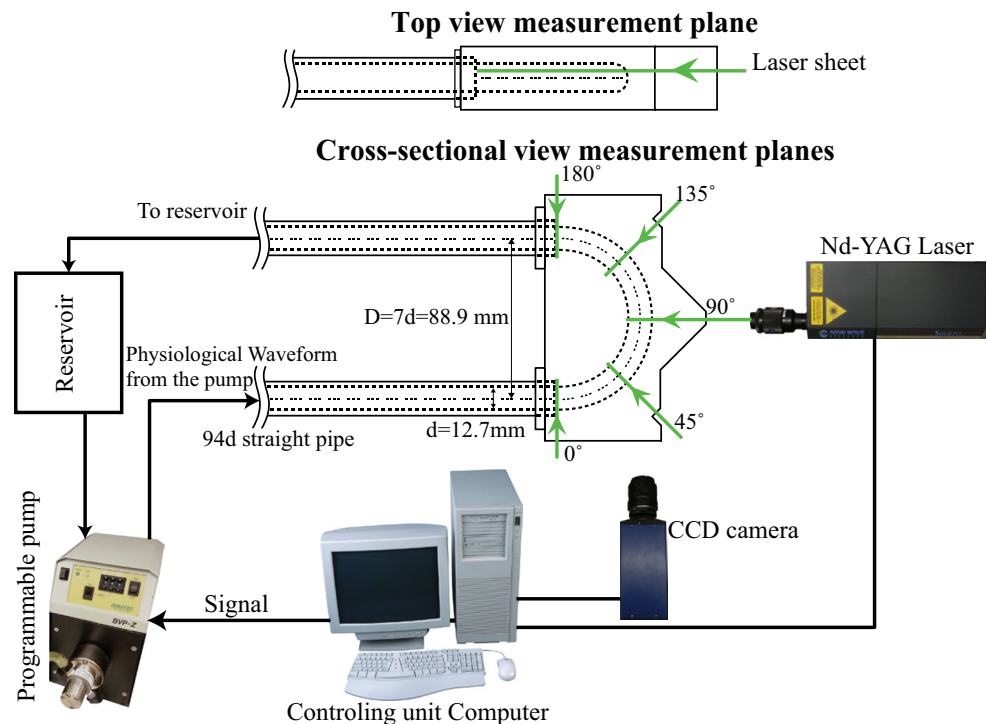
gradient force exceeds the centrifugal force before the peak flow rate, resulting in a stagnation point first occurring in the secondary flow, followed by Lyne vortex formation.

Timité et al. (2010) also studied axial velocity profiles and secondary flow in steady, oscillatory and pulsatile inflow conditions both numerically (Fluent 6 software) and experimentally by a laser Doppler velocimetry technique. They observed the additional vortex pair for high Dean number in steady flow, similar to Soh and Berger (1984) and van Wyk et al. (2015), and attributed this to the proximity of the developing region. The effect of velocity amplitude ratio (β), the ratio of maximum oscillatory component to the mean component of pulsatile flow, was also investigated by Timité et al. (2010). They showed that (in agreement with Takami et al. 1984; Hamakiotes and Berger 1988) for $\beta < 1$ the flow structures are similar to the steady flow case, while for $\beta > 1$ the flow structures are more complex than Dean flow containing Lyne vortices. Huang et al. (2010) studied the pulsatile physiological flow in simplified normal and stenosed aortic arches including the three branch vessels using time-resolved particle image velocimetry (PIV). Using axial velocity and wall shear stress (WSS) data they observed a large separation bubble at inner wall due to the adverse streamwise pressure gradient. A recirculation zone upstream of the first branch was also observed at the outer wall during deceleration because of reverse flow from the branch, which caused a large WSS in that region.

In our laboratory, Glenn et al. (2012) studied physiological pulsatile flow (based on carotid artery waveform, see Holdsworth et al. 1999) using PIV in a curved tube with and without idealized stent-induced disturbances. They observed different secondary flow morphologies throughout the cardiac period: one, two and three symmetric pair(s) of vortical pattern including deformed-Dean, Dean, Wall and Lyne vortices. Proper orthogonal decomposition was applied, and a regime map for vortical structure based on secondary Reynolds number and acceleration parameter was proposed. This study was followed by Bulusu and Plesniak (2013) to examine disturbances induced by a realistic stent model. They applied two-dimensional Ricker wavelet analysis to the vorticity field to identify different vortical structures in secondary flow at 90° along the curve. All of the above-mentioned studies used Newtonian blood-analog fluid in their simulations and experiments, except van Wyk et al. (2015) who simulated pulsatile flow in curved pipe using both Newtonian and non-Newtonian (shear-thinning) models. They compared only their numerical Newtonian results with available experimental PIV data, with favorable results.

Pulsatile flow in a 180° curved tube is investigated in the present study due to its relevance in physiological flow, applications in industrial systems and existence of various

Fig. 1 Schematic of test section, laser sheet locations and camera direction for both top and cross-sectional views



secondary flow structures. Most of the studies on pulsatile flow in curved pipes have been focused on the velocity field with some attention paid to the vorticity fields. In general, there is a dearth of studies using vortical structure detection schemes to study the evolution of vortical structures in both time and space. High-resolution experimental data covering both the primary and secondary flow are essential to provide boundary and initial conditions for numerical simulation, as well as validation. The present study extends the understanding of flow in curved tubes by investigating the evolution of vortical structures in a curved artery model under both steady and physiological carotid artery (pulsatile) inflow waveform. A non-Newtonian working fluid is used to more realistically mimic physiological flows, and in-plane velocity fields are measured with high-resolution PIV (Sect. 2). A vortex detection algorithm is applied to both secondary and primary velocity field data to distinguish vortical structures from others (Sect. 3). Section 4 is devoted to velocity, vorticity and vortex detection results with discussion concerning flow structures, as well as circulation analysis and vortex locus results.

2 Experimental apparatus and methods

2.1 Test section geometry

The 180° curved tube was machined out of an acrylic block and polished to provide clear optical access. Unobstructed

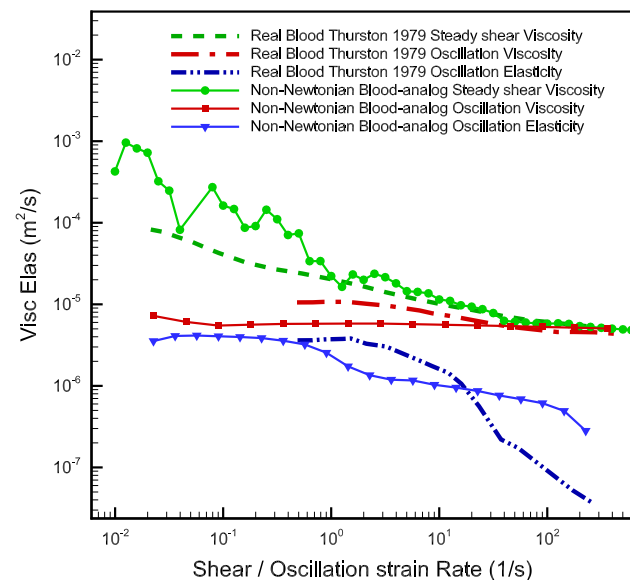
optical access for both top-view and cross-sectional view measurements required two different test sections (schematics are shown in Fig. 1). The inner diameter of pipe is $d = 12.7$ mm with a curvature ratio of $\delta = d/D = 1/7$. The cross-sectional measurements were made at 0°, 45°, 90°, 135° and 180° along the curve, and top-view measurements were taken at a plane 2.5 mm above the horizontal centerline of the pipe to cut through the secondary flow structures.

2.2 Blood-analog fluid rheology

Human blood is a complex fluid composed of various substances and particles, i.e., plasma, red and white blood cells, platelets and proteins. Therefore, it is important that a blood-analog fluid used for in vitro experiments has characteristics of real blood, as well as being optically clear and refractive index (RI) matched to the test section. Among many different compositions of non-Newtonian blood-analog fluid, those composed of xanthan gum-based mixtures are known to be the most stable and reliable ones (Naiki et al. 1995; Vlastos et al. 1997; Long et al. 2005). The composition of the working fluid in this study is listed in Table 1 and is based on Long et al. (2005). Furthermore, Long et al. (2005) noted that adding sodium iodide (NaI) for RI matching does not change the viscoelasticity of the fluid. Contrary to the comments made by Long et al. (2005), rheological measurements made in our laboratory revealed that adding more sodium iodide to the

Table 1 Non-Newtonian fluid composition and characteristics

Substance	Weight percentage (%)
Glycerin	14.2537
Xanthan gum	0.02673
Water	30.2623
Sodium iodide	55.4573
Density of fluid (Kg/m ³)	1678.29
Refractive index	1.494

**Fig. 2** Viscosity and elasticity of non-Newtonian blood-analog fluid in Table 1 and real blood data from Thurston (1979). The density of real blood assumed to be 1070 kg/m³

solution of glycerin, xanthan gum and water progressively decreases the non-Newtonian properties of the solution and leads to less shear-thinning/viscoelastic fluid (Najjari et al. 2016). However, because the refractive index of the fluid is a critical factor for obtaining high-quality particle image velocimetry (PIV) measurements, the blood-analog fluid used in this study contains more NaI than that of Long et al. (2005), to match the RI of our test section (RI = 1.495). This particular fluid is shear-thinning and weakly viscoelastic. Rheological properties of fluid used in current study were measured using a Discovery HR-2 (TA Instruments) rheometer under steady shear and oscillatory conditions at 2 Hz. The oscillatory mode is used to measure the storage and loss modulus of the fluid, which correspond to elasticity and viscosity, respectively. Figure 2 shows kinematic viscosities and elasticity variations with steady and oscillatory shear rate for our blood-analog fluid compared with real blood data from Thurston (1979). The viscosity decreases with increase in steady shear rate. This

Table 2 Details of PIV recording parameters

Laser	Nd:YAG New wave Solo III
Wavelength	532 nm
Energy	50 mJ/pulse
Camera	LaVision Imager Intense
Resolution	1376 × 1040 pixels
Pixel pitch	6.45 μm
Lens	Nikkor 50 mm with 20-mm extension tube
Lens aperture	f/8
Magnification factor	0.387
Seed particles	Fluorescent polymer microspheres (Flouro-Max)
Particle diameter	7 μm
Particle density	$\rho_p = 1.05\text{--}1.19 \text{ g/cm}^3$

demonstrates the shear-thinning property of the fluid that is in good agreement with kinematic viscosity of real whole blood.

2.3 Particle image velocimetry and image analysis

Phase-locked instantaneous velocity fields were measured using PIV. The PIV parameters are tabulated in Table 2. The slip velocity for particles can be estimated from Eq. (1) (Dong et al. 1992; Pedersen 2000).

$$\left(\frac{\Delta u}{u_f}\right)^2 = \left(\frac{\rho_p - \rho_f}{\rho_f}\right)^2 \frac{d_p^2 f_0}{9\nu_f} \quad (1)$$

where the time scale of the flow is $1/f_0 = d/V_{\text{bulkMax}} = 0.0127/0.45(\text{s})$ and $\nu_f \approx 5 \times 10^{-6} \text{ (m}^2/\text{s)}$. This leads to the maximum slip velocity of 0.23 %. In the top-view measurements, the 180° curved section is divided into eight fields of view (FOVs) with overlapping regions to increase spatial resolution. A two-axis traverse system is used to position the camera. In order to calibrate the camera, an in-house calibration map (Fig. 3) is mounted into the test section filled with RI-matched fluid. A third-order polynomial fit is used for calibration, to minimize any optical distortion in the images. The calibration map for top-view measurements also has the boundaries for each FOV including an overlap region, which is used for assigning coordinates to FOVs with respect to each other. Because the bulk velocity varies considerably for pulsatile flow, an optimum value of the time delay between successive laser pulses, dt , was determined at each phase to limit maximum particle displacement to 8 pixels. To ensure statistical convergence, 150 images pairs were acquired at each phase. DaVis 7.2 (LaVision) was used as the data acquisition and image post-processing software.

For image post-processing, the background image is first subtracted, and geometrical masking is then applied to the

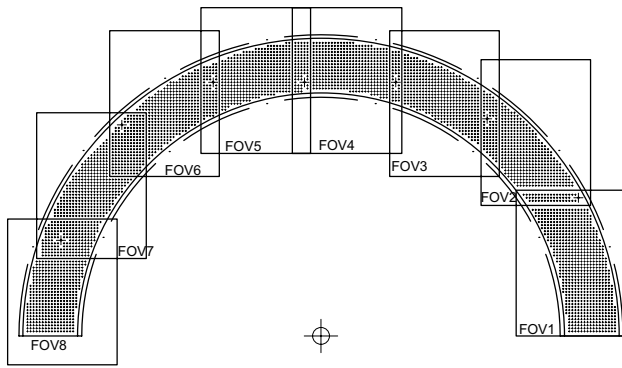


Fig. 3 Calibration map and field-of-view arrangement

images, followed by vector field calculation. A multi-pass option with decreasing window size from 64 pixels to 32 pixels with 50 % overlap is used for the interrogation area (IA). This results in ~ 0.27 and ~ 0.22 mm vector spacing and ~ 0.54 and ~ 0.44 mm spatial resolution for top-view and cross-sectional view measurements, respectively.

2.4 Inflow conditions

A 94 d length of straight pipe was attached to the inlet to minimize upstream effects and disturbances at the curved test section ($d = 12.7$ mm). The inflow waveforms were produced by a gear pump (Ismatec model BVP-Z) controlled by customized LabView virtual instrument and data acquisition card (NI DAQ Card-6024E). Table 3 lists inflow details for four steady flow rates and a physiological pulsatile flow used in the present study. The original pulsatile inflow waveform that was based on the common carotid artery flow rate (Holdsworth et al. 1999) was scaled in order to match the Womersley number to $\alpha = 4.2$ (Glenn et al. 2012; Bulusu and Plesniak 2013). Due to the shear-thinning property of the fluid, its viscosity changes throughout cycle. Therefore, maximum strain rate is first calculated upstream of the curve in the straight pipe, and then, the viscosity is chosen based on the corresponding strain rate from Fig. 2. Figures 4 and 5 show the pulsatile flow rate measured by an ultrasonic flowmeter

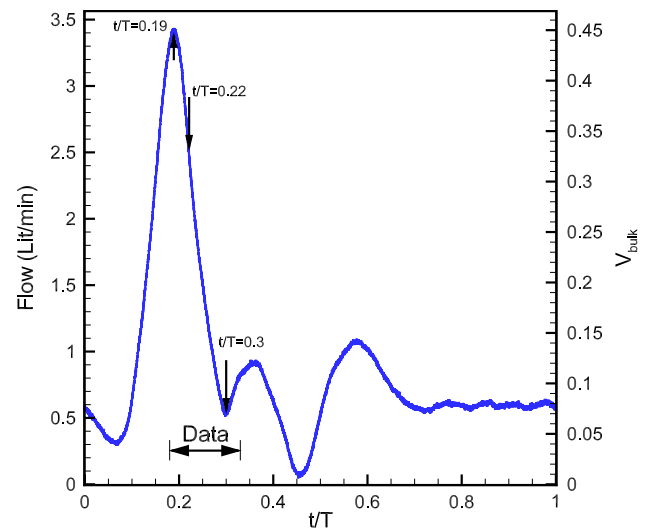


Fig. 4 Pulsatile carotid artery physiological waveform (Holdsworth et al. 1999). PIV data acquired between $t/T = 0.18$ and $t/T = 0.33$

(TRANSONIC ME12PXL) (downstream of the curve) and the phase-averaged centerline velocity profiles measured upstream of the curve using PIV, respectively. Although a long straight pipe is attached to the inlet of the test section, due to $\alpha \gg 1$ the inflow profile does not have enough time to achieve a parabolic (Poiseuille) shape, but the flow at entrance of the curve is fully developed (i.e., $\partial/\partial x = 0$). Due to a lag between pressure and velocity, reverse flow occurs in near wall regions at the end of systolic deceleration, $t/T = 0.3$, and late diastole period, $t/T = 0.45$ (Fig. 5).

2.5 Data post-processing and validation

The instantaneous velocity field provided by DaVis software is input to an in-house Fortran code, which is used for further post-processing. In addition to the validation criteria in DaVis 7.2, a statistical data validation method (Najjari et al. 2012, 2015) is applied to all PIV data to eliminate uncertainty and achieve convergence (achieved at 80 of 150 realizations for velocities). Figure 6a shows the convergence for velocity magnitude at different points in the 45° cross section. The vorticity convergence at multiple

Table 3 Flow parameters for pulsatile and four steady flow rates

Parameter	Pulsatile flow			Steady flow			
	Peak systole	Min systole	Min diastole	Case 1	Case 2	Case 3	Case 4
U_{bulk} (ms^{-1})	0.45	0.073	0.012	0.225	0.153	0.093	0.064
ϵ_{Max} (s^{-1})	280	75	35	110	70	45	30
ν (St)	0.050	0.053	0.054	0.052	0.053	0.053	0.054
$Re = U_{bulk} d/\nu$	1143	175	28	550	366	223	150
$De = Re\sqrt{\delta}$	432	66.1	10.6	208	138.2	84.5	56.6

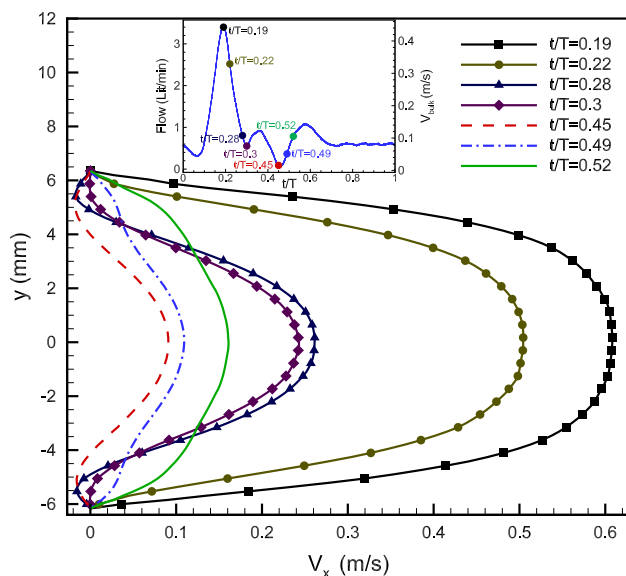


Fig. 5 Non-Newtonian fluid inflow centerline velocity profiles at different phases during pulsatile waveform measured upstream of the curve using PIV. The *inset* shows corresponding to the points on the waveform

points in the 90° cross section at $t/T = 0.29$ is also shown in Fig. 6b. The maximum variation of averages for the last 30 realizations is divided by the final value of the parameter and shown in percentages next to the each line. Points 2 and 1 in Fig. 6a, b, respectively, have high variations because the parameter magnitude is small. These results verify that satisfactory convergence is achieved within the number of realizations acquired.

To benchmark our PIV measurements, a Newtonian fluid was first tested in the same experimental setup and data upstream of the curve are compared with an analytical solution for this pulsatile flow. Figure 7¹ shows excellent agreement of the experimental data with the analytical solution. The analytical solution for the Newtonian pulsatile flow in the straight pipe is obtained using Laplace transform method (Das and Arakeri 1998, 2000; Volodko and Koliskina 2008). Using this method, the Navier–Stokes equations in cylindrical coordinate are solved for unsteady laminar flow conditions when the only nonzero velocity component is in the streamwise direction, which only varies with r . Details of analytical solution are provided in “Appendix.”

3 Vortex detection method

Two in-plane velocity components, u and v , are obtained from PIV corresponding to local x - and y -directions in each

¹ This is the only figure in the present study showing the Newtonian fluid results.

measurement plane. Therefore, the x - and y -directions in top-view measurements are different from those in cross-sectional measurements. The z -direction in all cases is the out-of-plane (normal to each measurement plane) direction, which varies between different cross sections and in the top view. In-plane spatial derivatives are calculated in the Fortran code using a central finite difference method. The d_2 -method (discriminant of non-real eigenvalues of velocity gradient matrix, Vollmers 2001) defined in Eq. (2) is used to identify the vortical structures in both primary and secondary flows. This is a Galilean-invariant method that distinguishes vortical structures from shear regions. A negative value of d_2 indicates a vortex region. The Fortran code also identifies individual distinct vortical structures in cross-sectional views to facilitate studying each vortex separately. The circulation ($\Gamma = \Delta x \Delta y \times \sum \omega_z$) is calculated for each vortical structure, where $\Delta x = \Delta y \approx 0.22$ mm and ω_z refers to out-of-plane vorticity. The summation is done over the area occupied by each vortex.

$$d_2 = \left(\frac{\partial u}{\partial x} + \frac{\partial v}{\partial y} \right)^2 - 4 \left(\frac{\partial u}{\partial x} \frac{\partial v}{\partial y} - \frac{\partial u}{\partial y} \frac{\partial v}{\partial x} \right) \quad (2)$$

4 Results and discussion

4.1 Velocity field

4.1.1 Steady flow

It is well established that steady flow through a curved pipe contains two symmetric, counter-rotating vortices, namely Dean vortices. In addition, Dennis and Ng 1982; Nandakumar and Masliyah 1982; Yanase et al. 1989; Mallubhotla et al. 2001; Tiwari et al. 2004; van Wyk et al. 2015 showed that, for Dean number higher than a critical value, additional vortices can form in the cross section of the curved pipe. van Wyk et al. (2015) reported a four- or six-vortex pattern in secondary flow at 90° under steady flow with conditions similar to cases 1 and 2 in the present study. Figure 8 shows velocity magnitude and axial velocity profiles for top view of steady flow for four different flow rates. For cases 1 and 2, in agreement with Soh and Berger (1984), there is a double peak and plateau in the axial velocity profiles at 90° associated with secondary flow structures other than Dean vortices. A similar double peak and plateau in axial velocity profile in pulsatile flow is a hallmark of Lyne vortices in the secondary flow. It is found that secondary and axial flow structures in steady flow are morphologically similar to those in pulsatile flow if the Dean number is high enough. Mallubhotla et al. (2001) and Tiwari et al. (2004) argued that the Dean vortex splits (bifurcates) into two structures in each half of the pipe and forms a four-vortex pattern. Other researchers reported that the *solutions bifurcate* at high De and *not* the structures (Dennis and Ng 1982;

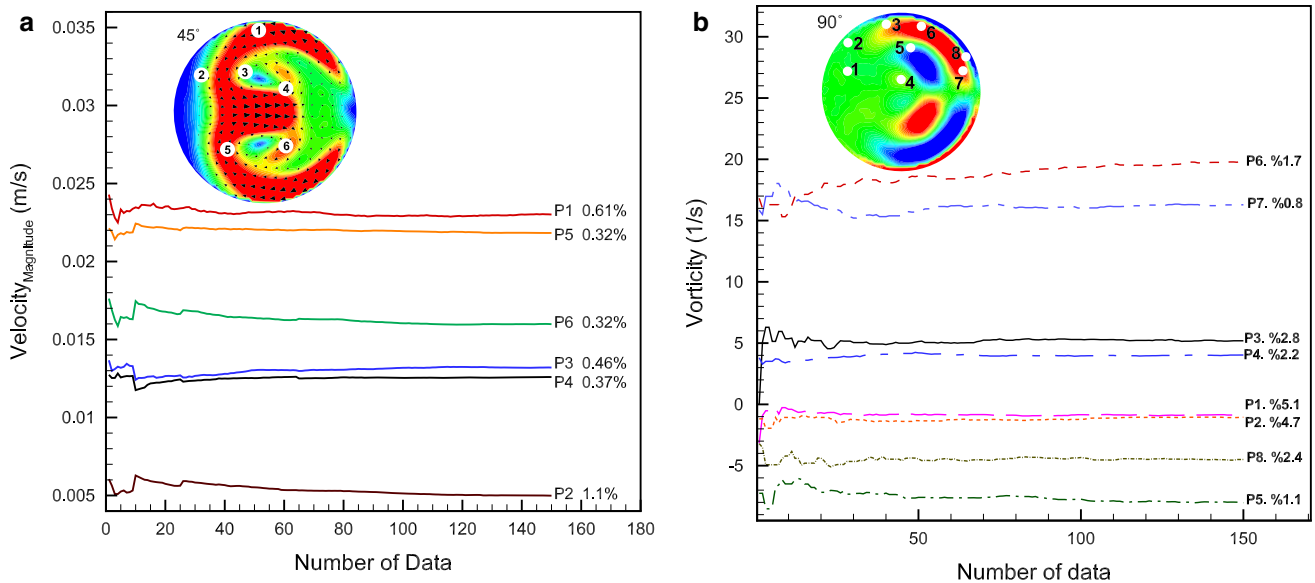


Fig. 6 Convergence diagram for **a** velocity at multiple points in 45° cross section and **b** vorticity at various points in the 90° cross section. The range of convergence for last 30 data realizations is shown in percentage

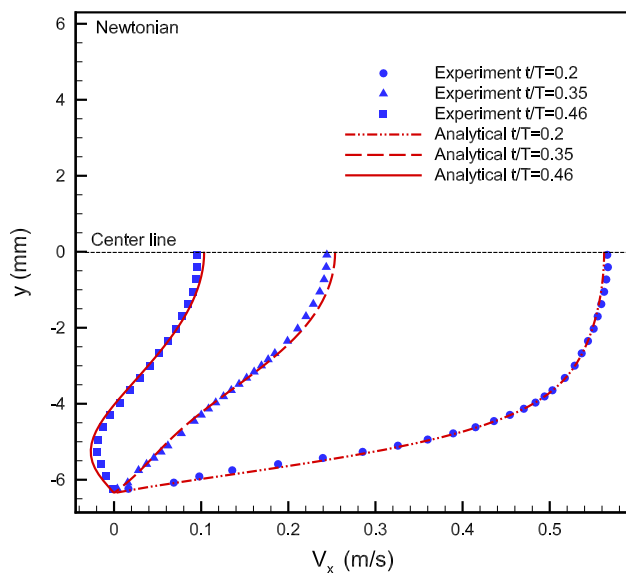


Fig. 7 Analytical solutions and PIV results for centerline velocity profiles upstream of the curve for Newtonian fluid at three different phases

Nandakumar and Masliyah 1982; Yanase et al. 1989). As the *De* increases, the radial pressure gradient forces, which act against the centrifugal forces along the line of symmetry, also increase. Therefore, a stagnation point forms (Fig. 9b), which pushes the Dean vortex closer to the wall, and the viscous region becomes more confined to the near wall, and hence, an inviscid core forms (Berger et al. 1983). The inviscid core is also evident from top-view velocity data, in which the plateau in the profile exists. For this condition,

the deformed-Dean vortices drag the inviscid core of the flow and form the counter-rotating vortices (Fig. 9c). As a result, two symmetrical vortex pairs (four-vortex pattern) can be observed. This is the same mechanism introduced by Lyne (1971) under oscillatory inflow conditions.

As the *De* is increased further, separation of secondary boundary layer starts from the inner wall and centrifugal forces act on deformed-Dean structures (Fig. 9d), causing the round-shaped head of deformed-Dean vortex to split from the elongated part and form a set of two additional structures shown in Fig. 9e (i.e., Dean and Wall vortices). This results in three symmetrical vortices, or six-vortex pattern, e.g. van Wyk et al. (2015) reported a six-vortex pattern for steady flow conditions. Therefore, multiple pairs of secondary flow vortices are reported under steady inflow conditions for sufficiently high *De*; they are not limited to oscillatory or pulsatile cases.

4.1.2 Pulsatile flow

The phase-averaged velocity fields are obtained using phase-locked PIV data. Figure 10 shows the top view and cross-sectional views at four instances during the systolic deceleration phase. The doubly-peaked axial velocity at 90°, *t/T* = 0.18, is a signature of the distorted secondary flow from Dean-type vortices and significant radial forces directed toward inner wall (Zalosh and Nelson 1973; Soh and Berger 1984; Hamakiotes and Berger 1988). During deceleration, the velocity profile is skewed toward the outer wall, which indicates the dominance of centrifugal forces over the radial pressure gradient forces, and the boundary

Fig. 8 Non-dimensional velocity magnitude and streamlines from top-view at 2.5 mm above the centerline for four different steady flows **a** $Re = 550$, **b** $Re = 366$, **c** $Re = 223$, **d** $Re = 150$ and axial velocity profiles for all cases at **e** 90° , **f** 45°

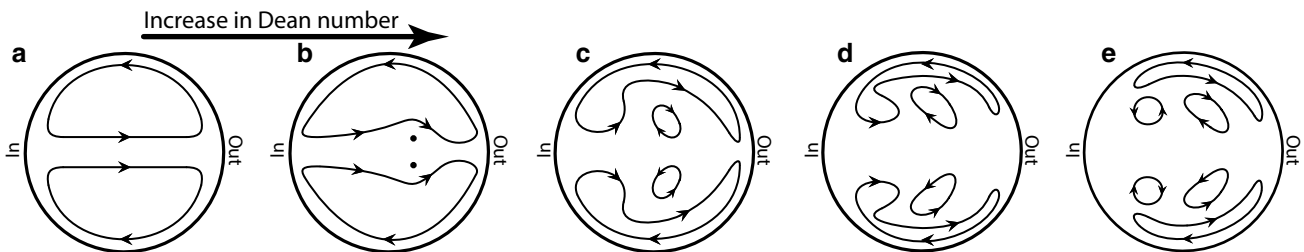
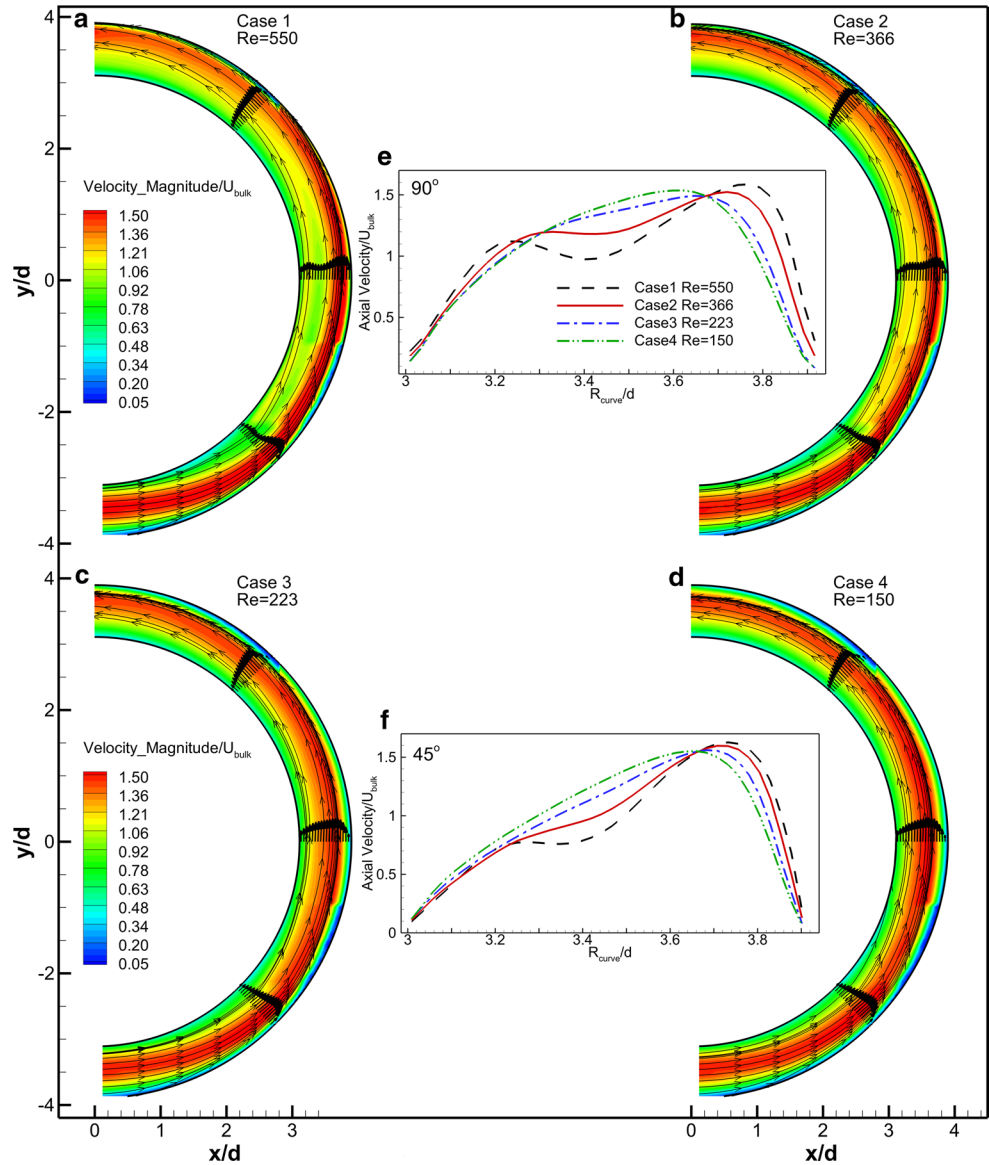


Fig. 9 Schematics of secondary flow structures under steady flow. The inner and outer wall are denoted by “In” and “Out,” respectively

layer at inner wall grows faster than that at the outer wall due to adverse pressure gradient caused by both flow deceleration and surface curvature. As the flow decelerates (Fig. 10b), the streamlines start to deviate and bend around the 45° location, and the flow tends to separate from the

inner wall upstream of the 45° location. At $t/T = 0.27$, as shown in Fig. 10c, two low-velocity regions exist in the initial section of the curve, one with closed streamlines revealing a vortical structure. This structure, also reported by Chandran and Yearwood (1981), Talbot and Gong

(1983), Huang et al. (2010), moves upstream and away from the inner wall as the flow decelerates. Near the end of the deceleration phase, as shown in Fig. 10d, the second vortical structure in the initial section of the curve can be observed by plotting streamlines. The formation of these initial vortical structures redirects the mean flow toward

the inner wall and forms a wall jet flow with high WSS immediately downstream of the low WSS region in separated flow. Phenomena accompanying WSS can cause or accelerate cardiovascular diseases, e.g., platelet activation, thrombosis and plaque disruption in high WSS regions (Giddens et al. 1990; Ku 1997) and atherosclerosis in low

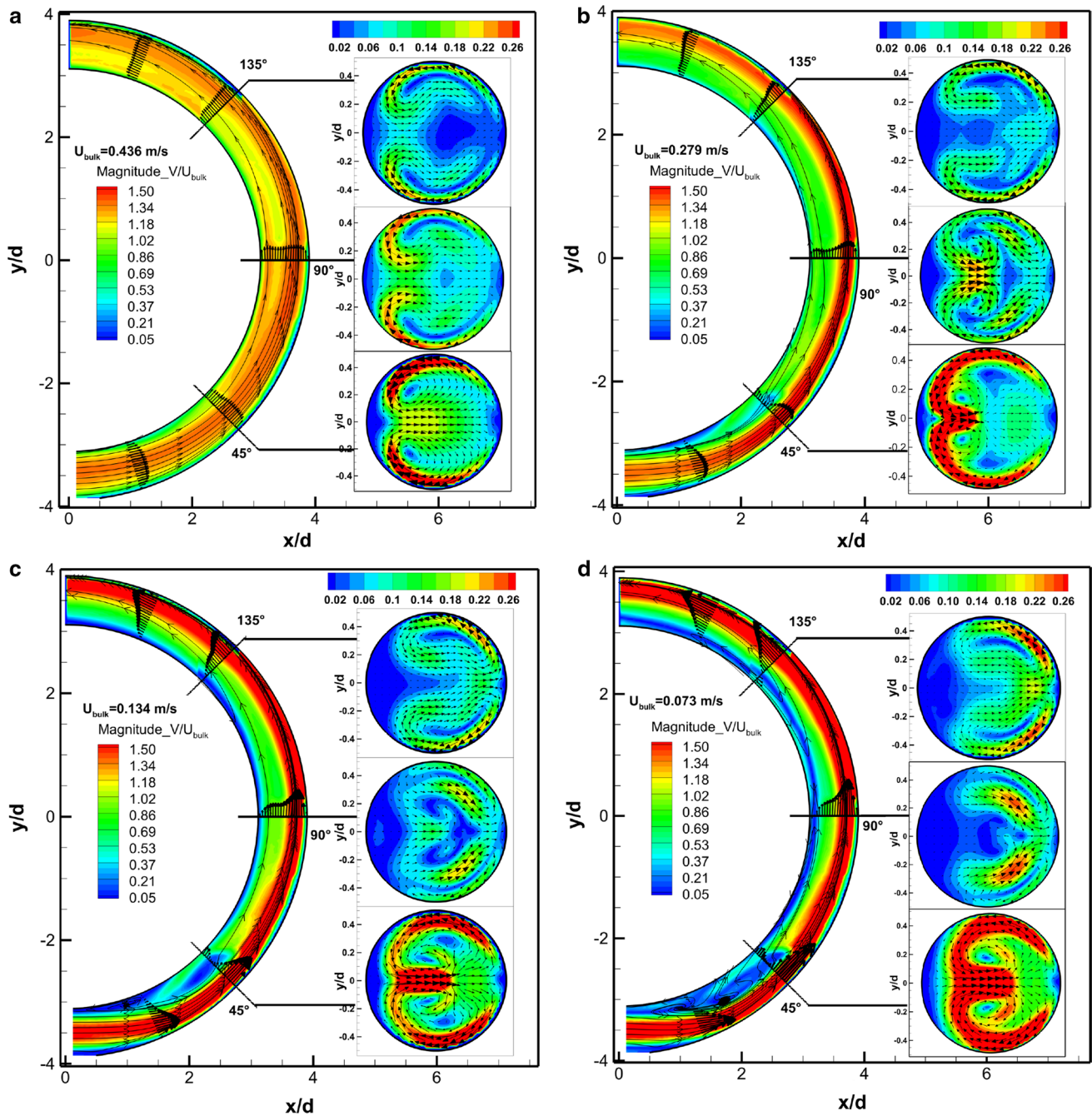


Fig. 10 Non-dimensional velocity magnitude and velocity vectors at 2.5 mm above the centerline for top view and three cross-sectional views for pulsatile physiological waveform at **a** $t/T = 0.18$, **b** $t/T = 0.23$, **c** $t/T = 0.27$, **d** $t/T = 0.30$. 1/3 of vectors are plotted for clarity

WSS region (Traub and Berk 1998; Malek et al. 1999; Stone et al. 2003). Moreover, drug particles or platelets may become trapped into these structures, causing serious disorders.

As discussed in Sect. 2, due to the phase lag between pressure and velocity, flow reversal occurs near the walls of the straight pipe section at the end of flow deceleration. In the curved pipe, due to acceleration of flow toward the outer wall, no reversed flow is observed at outer wall, while at $t/T = 0.29$ and 0.3 reversed flow exists only in the vicinity of inner wall downstream of 45° up to the end of the curve. Similar reversed flow near the inner wall was also reported by Hamakiotes and Berger (1988), Naruse and Tanishita (1996), Boiron et al. (2007), Timité et al. (2010). Flow separation from the inner wall results in the formation of another vortical structure downstream of 135° .

The cross-sectional views in Fig. 10 reveal different coherent structures visualized by streamlines. These structures, i.e., Dean (D), deformed-Dean (DD), Lyne² (L) and Wall (W)-type vortices, are well established in the literature (Sudo et al. 1992; Bulusu and Plesniak 2013) and will be discussed in next section.

4.2 Identification of vortical structures

In order to study the evolution of vortical structures in the curve, d_2 is computed for top and cross-sectional view data, with negative regions of d_2 plotted in Fig. 11. The threshold for showing vortical regions is chosen to be 0.1 % of minimum d_2 , i.e., regions where $d_2 > -0.01 \times \text{Max}\{-d_2\}$ were blanked out. At $t/T = 0.18$ (Fig. 11a), a vortical structure exists at initial section of the curve due to adverse (streamwise) pressure gradient. This structure then splits into two parts around the 45° location. The vorticity field shows that the split occurs at the zero vorticity location, which is consistent with the requirement that vortex tubes cannot split or join within the flow unless the vorticity is zero (Panton 2005). After the initial vortex split, the right branch downstream of the 45° location shows position of the Lyne vortex and the white region in between two branches shows the location of Dean vortex. The normal component of vorticity for the top view at $t/T = 0.18$ is also shown in Fig. 12. Similar to d_2 a split in the vorticity structure can also be observed upstream of 45° ; however, the vorticity in the right branch weakens downstream. Therefore, based on d_2 -analysis, Lyne vortices are most probably connected to structures upstream of 45° where vorticity has a significant component normal to the top-view plane. As the flow develops along the curve,

the axis of vorticity/vortex rotates and gains a component normal to the cross-sectional plane. During the deceleration, the vortical structure upstream of 45° moves toward the outer wall, the splitting point moves upstream and the left branch of vortical structure separates from the inner wall and moves closer to the center of the pipe. The current data do not reveal information on this left branch—it might be a structure near the inner wall or the artifact of d_2 in two-dimensional data near the curved wall.

The d_2 -plots for cross-sectional planes show different coherent structures, namely deformed-Dean, Dean, Wall and Lyne at different phases. The terminology “deformed-Dean” refers to the structure when the Dean and Wall-type vortices are attached, e.g., Figure 11a 45° , 90° and 135° . While the flow decelerates, the deformed-Dean vortex system persists at 45° and moves toward the outer wall; at 90° , the Dean vortex separates from the Wall-type vortex forming a distinct 4-vortex system in addition to Lyne vortex pair. The Dean vortex pair then moves toward the outer wall and decays at $t/T = 0.3$. While the flow develops along the curve, the Dean vortices rejoin the Wall-type vortices around 135° reverting to the original deformed-Dean system. The Lyne vortices are formed prior to the systolic peak ($t/T = 0.18$)—when the pressure forces are dominant over the centrifugal forces—and persist during deceleration downstream of 45° , at 90° and 135° . This result agrees with Boiron et al. (2007), who computed the centrifugal forces and radial pressure gradient and showed that immediately before the peak flow, the radial pressure gradient dominates the centrifugal forces, and hence, stagnation regions and Lyne vortices form. At 135° , each Lyne vortex splits into two parts that are rejoined during the rest of systole deceleration phase.

Based on the idea that several vortex tubes exist in the curved pipe, circulation analysis is done to investigate the spatial relation of structures along the curve and also in time. Figure 13 shows the circulation (Γ) for different structures in top half of cross-sectional views. All of the structures decay during deceleration, with the exception of Lyne vortices, which first gain energy and then weaken during the period. We hypothesize that because the Lyne vortex does not form as a direct result of imbalance between pressure and centrifugal forces, but rather because the viscous region drags the inviscid core, this process needs some time to develop. Therefore, the Lyne vortex system is in its formation phase so it gains strength. Cross-sectional views in Fig. 10 show that the deformed-Dean vortices at 45° develop along the curve and also exist at 90° at $t/T = 0.18$. The Γ for these structures at 45° and 90° do not match exactly, but are within a factor of $\Gamma_{90^\circ}/\Gamma_{45^\circ} \simeq 85 - 50\%$. A possible explanation is that planar PIV only captures the vorticity normal to the plane, and thus, the Γ calculated represents only a fraction of the vortex tube strength.

² Here the terminology “Lyne vortex” refers to the deformed-Lyne vortex based on Sudo et al. (1992).

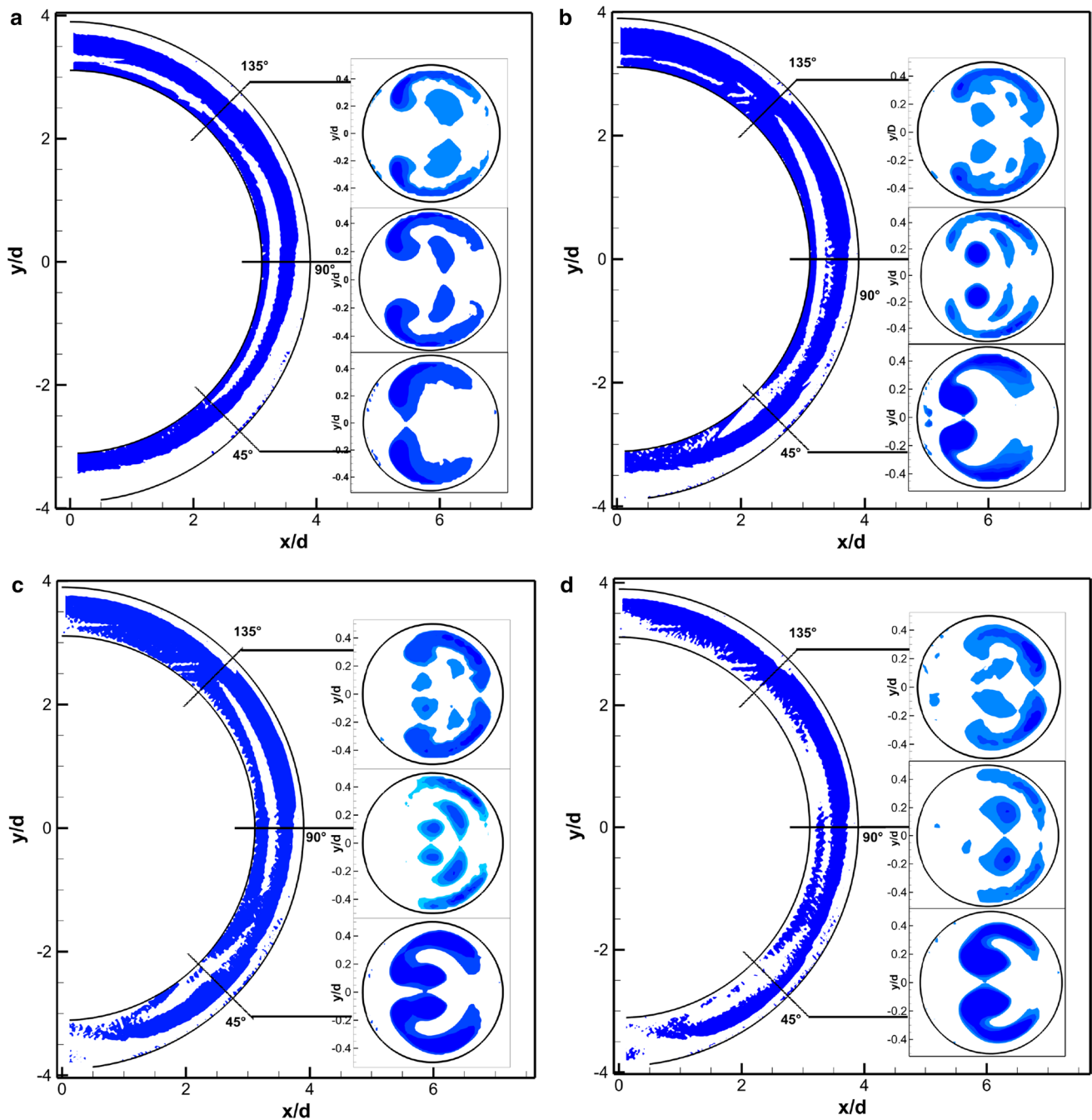


Fig. 11 Negative region of d_2 (vortex regions) for top view and cross-sectional views for pulsatile physiological waveform at **a** $t/T = 0.18$, **b** $t/T = 0.23$, **c** $t/T = 0.27$, **d** $t/T = 0.30$

Later in time, $t/T = 0.22$, after the Wall and Dean vortices exist separately at 90° the sum of Γ for both (shown by * in Fig. 13a) follows the trend of the deformed-Dean, suggesting that the deformed-Dean vortex at 45° splits into Dean and Wall vortices upstream of 90° . In addition, after each Lyne vortex splits into two parts at 135° , the individual circulations, Γ , of the two parts sum to the total circulation

of the single Lyne vortex before splitting, as shown in Fig. 13b.

4.3 Locus of vortices

The approximate location of the vortex centers is obtained by finding the peak of $-d_2$ in each vortex

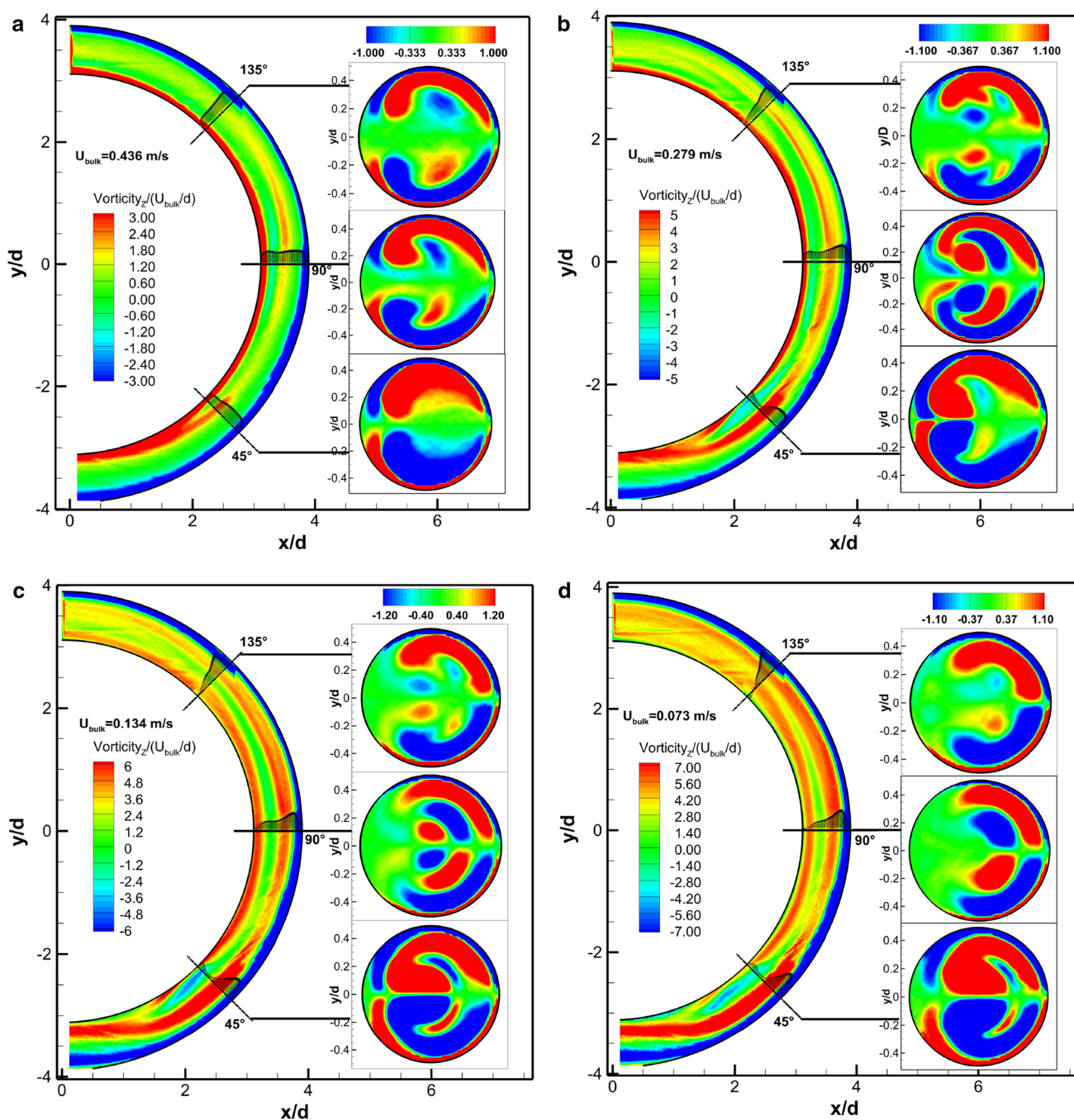


Fig. 12 Non-dimensional vorticity field and axial velocity profiles at 2.5 mm above the centerline for top view and three cross-sectional views for pulsatile physiological waveform at **a** $t/T = 0.18$, **b** $t/T = 0.23$, **c** $t/T = 0.27$, **d** $t/T = 0.30$

region. The centers then tracked through systole deceleration and plotted in Fig. 14, which shows the general path of different vortices in the 90° cross-sectional plane. After the deformed-Dean vortices split to form Dean and Wall vortices, the Dean part moves away from the inner wall and toward the center almost along a linear trajectory; the Wall vortex moves along the tube wall toward the line of symmetry. On the other hand, the center of

Lyne vortex moves in a circular path in the core region of the pipe.

5 Summary and conclusions

The primary and secondary flow under steady and pulsatile inflow in a 180° curved pipe was measured using PIV. A

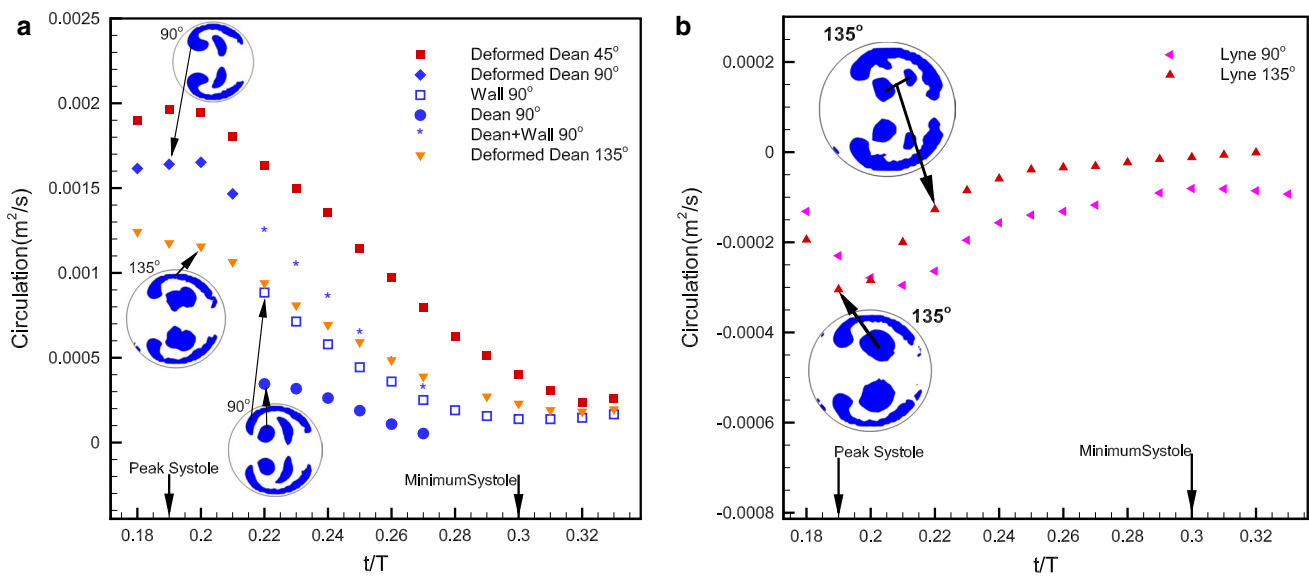


Fig. 13 Circulation (vortex strength) during systolic deceleration for different vortices in 45°, 90° and 135° cross sections: **a** deformed-Dean, Dean and Wall, **b** Lyne

shear-thinning, weakly viscoelastic non-Newtonian fluid is used as a blood-analog fluid to extend our previous studies (Glenn et al. 2012; Bulusu and Plesniak 2013; van Wyk et al. 2015). The phase-averaged velocity and vorticity fields are investigated to gain insight into the morphology, evolution and spatial development of vortical structures along the curved test section. A vortex detection method, d_2 , is used to identify the vortical structures in flow. The locus of secondary flow structures is found, and circulation analysis was performed. The main findings of the present study are:

Steady flow

- A doubly peaked axial velocity is observed for $De = 208$, which indicates a highly distorted secondary flow that contains an extra vortex pair(s) in addition to the canonical Dean vortices
- The formation mechanism of the counter-rotating extra vortices in the steady case is similar to that of Lyne vortices in pulsatile/oscillatory flow
- The primary flow tends to separate from the inner wall at high De , but no separation is observed at $De = 208$

Pulsatile flow

- Up to three vortex pairs are observed in the secondary flow field, i.e., Dean, Wall and Lyne vortices
- The secondary flow vortices at 90° and 135° split and rejoin both in time and space:

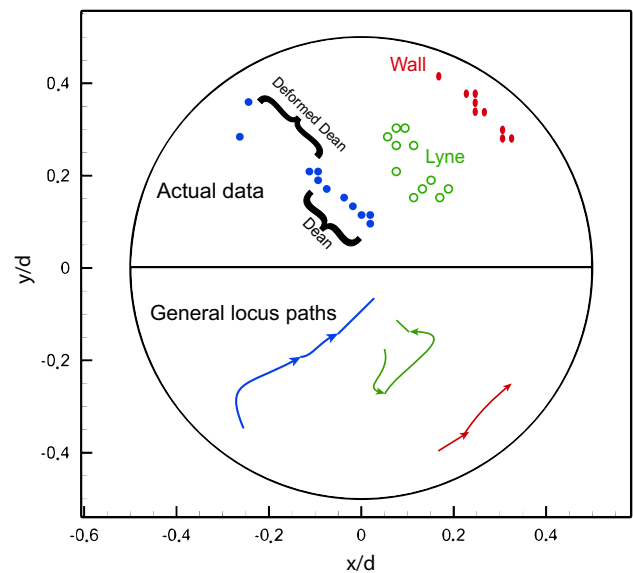


Fig. 14 Locus paths during systolic deceleration for different vortices at 90° cross section

- At approximately 90°, each deformed-Dean vortex splits into two structures during deceleration (Dean and Wall); subsequently, the two structures rejoin downstream of about 135° at the same phase
- Each Lyne vortex at 135° also splits into two structures that also rejoin during deceleration

- The separated Dean vortices at 90° move toward the outer wall during deceleration mostly due to the phase lag between pressure and velocity, which causes imbalance between centrifugal forces and radial pressure gradient forces. These structures decay at the end of deceleration phase.
- The d_2 field in the top view reveals that the initial longitudinal vortex in the primary flow splits into two structures at about 45° and the splitting point moves upstream during deceleration
- At the end of systolic deceleration, a separation bubble (recirculation zone) is observed in the initial section of the curve between ~10° and ~35°
- The circulation/vortex tube strength is calculated for each vortical structure in secondary flow and reveals that all structures are weakened during flow deceleration, except the Lyne vortex at 90° which first gains energy and then weakens

We note that the morphologies of the secondary flow structures in the current experiment with a non-Newtonian blood-analog fluid are very similar to those reported in our previous studies using a Newtonian blood-analog fluid (Glenn et al. 2012; Bulusu and Plesniak 2013; van Wyk et al. 2015). As discussed previously, the fluid is shear-thinning and weakly viscoelastic. For the (relatively large) flow rates experienced in large arteries, the shear-thinning properties of blood rheology do not affect the morphology of secondary flow structures. The effects of greater viscoelasticity on the secondary flow morphology are not expected to be significant either (Gijssen et al. 1999). This will be examined in follow-up experiments that will allow us to assess whether rheological properties of blood that are important in hemodynamics, transport and function affect the secondary flows significantly.

Appendix: Analytical solution for physiological pulsatile flow a straight pipe

Equations (3–6) are the governing momentum equation in cylindrical coordinates, boundary and initial conditions and mass flux, respectively. The nonzero initial condition (Eq. 5) is obtained from a parabolic fit to the flow rate at the end of the cycle and is used to eliminate the transient effect faster. The velocity, u_{bulk} , on right-hand side of Eq. (6) was calculated from a 28-Fourier mode fit to experimental flow rate obtained by an ultrasonic flowmeter. This equation allows omission of the pressure term from calculations.

$$\frac{\partial u}{\partial t} = -\frac{1}{\rho} \frac{\partial p}{\partial x} + \nu \left(\frac{\partial^2 u}{\partial r^2} + \frac{1}{r} \frac{\partial u}{\partial r} \right) \tag{3}$$

$$u(R, t) = 0 \quad \left. \frac{\partial u}{\partial r} \right|_{r=0,t} = 0 \tag{4}$$

$$u(r, 0) = a + cr^2 \quad a = 0.1366, \quad c = -a/R^2 \tag{5}$$

$$\int_0^R 2\pi r u(r, t) dr = u_{\text{bulk}}(t) \pi R^2 \tag{6}$$

A Laplace transform is applied to Eqs. (3–6) to convert partial differential equation to ordinary differential equation. For brevity, only transformed form of Eqs. (3 and 6) is provided in Eqs. (7 and 8). The overbar ($\bar{}$) denotes Laplace transform.

$$\frac{d^2 \bar{u}(r, s)}{dr^2} + \frac{1}{r} \frac{d\bar{u}(r, s)}{dr} - \frac{s}{\nu} \bar{u}(r, s) = \frac{1}{\mu} \frac{d\bar{p}(x, s)}{dx} - \frac{1}{\nu} u(r, 0) \tag{7}$$

$$\int_0^R r \bar{u}(r, s) dr = \frac{1}{2} \bar{u}_{\text{bulk}}(s) R^2 \tag{8}$$

The solution to Eq. (7) is given in Eq. (9)

$$\bar{u}(r, s) = C_1 I_0 \left(r \sqrt{s/\nu} \right) + Ar^2 + D \tag{9}$$

where $C_1 = -\frac{AR^2 + D}{I_0(R\sqrt{s/\nu})}$, $A = \frac{c}{s}$, $D = \frac{4c\nu}{s^2} - \frac{\phi\nu}{s} + \frac{a}{s}$, $\phi = \frac{1}{\mu} \frac{d\bar{p}(x, s)}{dx}$ and I_0 is the modified Bessel function of zeroth-order first kind. The only unknown in Eq. (9) is ϕ . By substituting $\bar{u}(r, s)$ from Eq. (9) into Eq. (8), ϕ can be calculated. Therefore, Eq. (9) gives the Laplace transform of the velocity profile. In order to invert the $\bar{u}(r, s)$ to obtain an expression for the physical velocity profile, a numerical approach was employed because of complexity of the analytical form. An open-source MATLAB code “Numerical inverse Laplace transform” McClure (2013) based on the Talbot algorithm (Abate and Whitt 2006) is used to perform the inversion. The optimum value for the parameter M (precision) in the code was chosen to ensure that calculated velocity profile satisfies the flow rate at each phase. The slight differences ($|\Delta u|/u_{\text{center}} = 0.3\text{--}8\%$) between the experimental result and the analytical solution in Fig. 7 are mainly due to errors implicit in the Laplace inversion numerical scheme.

References

Abate J, Whitt W (2006) A unified framework for numerically inverting Laplace transforms. *Inform J Comput* 18:408–421
 Berger SA, Talbot L, Yao L-S (1983) Flow in curved pipes. *Annu Rev Fluid Mech* 15:461–512
 Bertelsen AF (1975) An experimental investigation of low Reynolds number secondary streaming effects associated with an oscillating viscous flow in a curved pipe. *J Fluid Mech* 70:519–527

- Boiron O, Deplano V, Pelissier R (2007) Experimental and numerical studies on the starting effect on the secondary flow in a bend. *J Fluid Mech* 574:109–129. doi:[10.1017/S0022112006004149](https://doi.org/10.1017/S0022112006004149)
- Bulusu KV, Plesniak MW (2013) Secondary flow morphologies due to model stent-induced perturbations in a 180° curved tube during systolic deceleration. *Exp Fluids*. doi:[10.1007/s00348-013-1493-7](https://doi.org/10.1007/s00348-013-1493-7)
- Chandran KB, Yearwood TL (1981) Experimental study of physiological pulsatile flow in a curved tube. *J Fluid Mech* 111:59–85. doi:[10.1017/S0022112081002292](https://doi.org/10.1017/S0022112081002292)
- Das D, Arakeri JH (1998) Transition of unsteady velocity profiles with reverse flow. *J Fluid Mech* 374:251–283
- Das D, Arakeri JH (2000) Unsteady laminar duct flow with a given volume flow rate variation. *J Appl Mech* 67:274–281
- Dean WR (1927) Note on the motion of fluid in a curved pipe. *London Edinburgh Dublin Philos Mag J Sci* 4:208–223
- Dean WR (1928) The stream-line motion of fluid in a curved pipe. *London Edinburgh Dublin Philos Mag J Sci* 5:673–695
- Dennis SCR, Ng M (1982) Dual solutions for steady laminar flow through a curved tube. *Q J Mech Appl Math* 35:305–324
- Dong R, Chu S, Katz J (1992) Quantitative visualization of the flow within the volute of a centrifugal pump. Part A: technique. *J Fluids Eng* 114:390–395
- Eckmann DM, Grotberg JB (1988) Oscillatory flow and mass transport in a curved tube. *J Fluid Mech* 188:509–527
- Giddens DP, Zarins CK, Glagov S (1990) Response of arteries to near-wall fluid dynamic behavior. *Appl Mech Rev* 43:S98–S102
- Gijzen FJ, van de Vosse FN, Janssen JD (1999) The influence of the non-Newtonian properties of blood on the flow in large arteries: steady flow in a carotid bifurcation model. *J Biomech* 32:601–608. doi:[10.1016/S0021-9290\(99\)00015-9](https://doi.org/10.1016/S0021-9290(99)00015-9)
- Glenn AL, Bulusu KV, Shu F, Plesniak MW (2012) Secondary flow structures under stent-induced perturbations for cardiovascular flow in a curved artery model. *Int J Heat Fluid Flow* 35:76–83. doi:[10.1016/j.ijheatfluidflow.2012.02.005](https://doi.org/10.1016/j.ijheatfluidflow.2012.02.005)
- Hamakiotes CC, Berger SA (1988) Fully developed pulsatile flow in a curved pipe. *J Fluid Mech* 195:23–55. doi:[10.1017/S0022112088002319](https://doi.org/10.1017/S0022112088002319)
- Holdsworth DW, Norley CJ, Frayne R, Steinman DA, Rutt BK (1999) Characterization of common carotid artery blood-flow waveforms in normal human subjects. *Physiol Meas* 20:219–240. doi:[10.1088/0967-3334/20/3/301](https://doi.org/10.1088/0967-3334/20/3/301)
- Huang RF, Yang TF, Lan YK (2010) Pulsatile flows and wall-shear stresses in models simulating normal and stenosed aortic arches. *Exp Fluids* 48:497–508. doi:[10.1007/s00348-009-0754-y](https://doi.org/10.1007/s00348-009-0754-y)
- Jarrahi M, Castelain C, Peerhossaini H (2011) Laminar sinusoidal and pulsatile flows in a curved pipe. *J Appl Fluid Mech* 4:21–26
- Ku DN (1997) Blood flow in arteries. *Annu Rev Fluid Mech* 29:399–434
- Long J, Undar A, Manning KB, Deutsch S (2005) Viscoelasticity of pediatric blood and its implications for the testing of a pulsatile pediatric blood pump. *ASAIO J* 51:563–566. doi:[10.1097/01.mat.0000180353.12963.f2](https://doi.org/10.1097/01.mat.0000180353.12963.f2)
- Lyne WH (1971) Unsteady viscous flow in a curved pipe. *J Fluid Mech* 45:13–32. doi:[10.1017/S0022112071002970](https://doi.org/10.1017/S0022112071002970)
- Malek AM, Alper SL, Izumo S (1999) Hemodynamic shear stress and its role in atherosclerosis. *J Am Med Assoc* 282:2035–2042
- Mallubhotla H, Belfort G, Edelstein WA, Early TA (2001) Dean vortex stability using magnetic resonance flow imaging and numerical analysis. *AICHE J* 47:1126–1140. doi:[10.1002/aic.690470519](https://doi.org/10.1002/aic.690470519)
- McClure T (2013) Numerical Inverse Laplace Transform. In: MathWorks, Inc. <http://www.mathworks.com/matlabcentral/fileexchange/39035-numerical-inverse-laplace-transform>
- Mullin T, Greated CA (1980) Oscillatory flow in curved pipes. Part 2. The fully developed case. *J Fluid Mech* 98:397–416
- Naiki T, Yanai Y, Hayabashi K (1995) Evaluation of high polymer solutions as blood analog fluid. *J Jpn Soc Biorheol* 9:84–89
- Najjari MR, Montazerin N, Akbari G (2012) Statistical PIV data validity for enhancement of velocity driven parameters in turbomachinery jet-wake flow. In: 20th Annual international conference on mechanical engineering-ISME2012. Shiraz, Iran
- Najjari MR, Montazerin N, Akbari G (2015) On the presence of spectral shortcut in the energy budget of an asymmetric jet-wake flow in a forward-curved centrifugal turbomachine as deduced from SPIV measurements. *J Turbul* 16:503–524
- Najjari MR, Hinke JA, Bulusu KV, Plesniak MW (2016) On the rheology of refractive-index-matched, non-Newtonian blood-analog fluids for PIV experiments. *Exp Fluids* 57(6):1–6. doi:[10.1007/s00348-016-2185-x](https://doi.org/10.1007/s00348-016-2185-x)
- Nandakumar K, Masliyah JH (1982) Bifurcation in steady laminar flow through curved tubes. *J Fluid Mech* 119:475–490. doi:[10.1017/S002211208200144X](https://doi.org/10.1017/S002211208200144X)
- Naruse T, Tanishita K (1996) Large curvature effect on pulsatile entrance flow in a curved tube: model experiment simulating blood flow in an aortic arch. *J Biomech Eng* 118:180–186. doi:[10.1115/1.2795957](https://doi.org/10.1115/1.2795957)
- Panton RL (2005) Incompressible flow. Wiley, New Jersey
- Pedersen N (2000) Experimental investigation of flow structures in a centrifugal pump impeller using particle image velocimetry. Technical University of Denmark
- Shahcheraghi N, Dwyer HA, Cheer AY, Barakat AI, Rutaganira T (2002) Unsteady and three-dimensional simulation of blood flow in the human aortic arch. *J Biomech Eng* 124:378. doi:[10.1115/1.1487357](https://doi.org/10.1115/1.1487357)
- Siggers JH, Waters SL (2005) Steady flows in pipes with finite curvature. *Phys Fluids* 17:1–18. doi:[10.1063/1.1955547](https://doi.org/10.1063/1.1955547)
- Soh W, Berger S (1984) Laminar entrance flow in a curved pipe. *J Fluid Mech* 148:109–135. doi:[10.1017/S0022112084002275](https://doi.org/10.1017/S0022112084002275)
- Stone PH, Coskun AU, Kinlay S, Clark ME, Sonka M et al (2003) Effect of endothelial shear stress on the progression of coronary artery disease, vascular remodeling, and in-stent restenosis in humans in vivo 6-month follow-up study. *Circulation* 108:438–444
- Sudo K, Sumida M, Yamane R (1992) Secondary motion of fully developed oscillatory flow in a curved pipe. *J Fluid Mech* 237:189–208. doi:[10.1017/S0022112092003380](https://doi.org/10.1017/S0022112092003380)
- Takami T, Sudou K, Sumida M (1984) Pulsating flow in curved pipes: 1st Report, numerical and approximate analyses. *Bull JSME* 27:2706–2713
- Talbot L, Gong KO (1983) Pulsatile entrance flow in a curved pipe. *J Fluid Mech* 127:1–25. doi:[10.1017/S002211208300258X](https://doi.org/10.1017/S002211208300258X)
- Thurston GB (1979) Rheological parameters for the viscosity, viscoelasticity and thixotropy of blood. *Biorheology* 16:149–162
- Timité B, Castelain C, Peerhossaini H (2010) Pulsatile viscous flow in a curved pipe: effects of pulsation on the development of secondary flow. *Int J Heat Fluid Flow* 31:879–896. doi:[10.1016/j.ijheatfluidflow.2010.04.004](https://doi.org/10.1016/j.ijheatfluidflow.2010.04.004)
- Tiwari P, Antal SP, Burgoyne A, Belfort G, Podowski MZ (2004) Multifield computational fluid dynamics model of particulate flow in curved circular tubes. *Theor Comput Fluid Dyn* 18:205–220. doi:[10.1007/s00162-004-0127-3](https://doi.org/10.1007/s00162-004-0127-3)
- Traub O, Berk BC (1998) Laminar shear stress mechanisms by which endothelial cells transduce an atheroprotective force. *Arterioscler Thromb Vasc Biol* 18:677–685
- van Wyk S, Prah Wittberg L, Bulusu KV, Fuchs L, Plesniak MW (2015) Non-Newtonian perspectives on pulsatile blood-analog flows in a 180° curved artery model. *Phys Fluids*. doi:[10.1063/1.4923311](https://doi.org/10.1063/1.4923311)
- Vlastos G, Lerche D, Koch B, Samba O, Pohl M (1997) The effect of parallel combined steady and oscillatory shear flows on blood and polymer solutions. *Rheol Acta* 36:160–172

- Vollmers H (2001) Detection of vortices and quantitative evaluation of their main parameters from experimental velocity data. *Meas Sci Technol* 12:1199–1207
- Volodko I, Koliskina V (2008) Transient Flows in Pipes and Channels : Analytical Solutions. In: 4th IASME/WSEAS international conference on energy, environment, ecosystems and sustainable development, pp 265–268
- Yanase S, Goto N, Yamamoto K (1989) Dual solutions of the flow through a curved tube. *Fluid Dyn Res* 5:191–201. doi:[10.1016/0169-5983\(89\)90021-X](https://doi.org/10.1016/0169-5983(89)90021-X)
- Zalosh RG, Nelson WG (1973) Pulsating flow in a curved tube. *J Fluid Mech* 59:693–705